Lu *et al. Energy Mater* 2024;4:400038
**DOI:** 10.20517/energymater.2023.117

**Energy Materials**

**Article**

**Open Access**

Check for updates

# Modulating the graphitic domains of hard carbons via tuning resin crosslinking degree to achieve high rate and stable sodium storage

**Zhixiu Lu, Xiuping Yin, Yelin Ji, Caixia Li, Ruixiao Wang, Shenqi Li, Tao Yuan, Yufeng Zhao***

College of Sciences & Institute for Sustainable Energy, Shanghai University, Shanghai 200444, China.

***Correspondence to:** Prof. Yufeng Zhao, College of Sciences & Institute for Sustainable Energy, Shanghai University, 99 Shangda Road, BaoShan District, Shanghai 200444, China. E-mail: yufengzhao@shu.edu.cn

**How to cite this article:** Lu Z, Yin X, Ji Y, Li C, Wang R, Li S, Yuan T, Zhao Y. Modulating the graphitic domains of hard carbons via tuning resin crosslinking degree to achieve high rate and stable sodium storage. *Energy Mater* 2024;4:400038. https://dx.doi.org/10.20517/energymater.2023.117

**Received:** 26 Dec 2023 **First Decision:** 30 Jan 2024 **Revised:** 3 Apr 2024 **Accepted:** 3 Apr 2024 **Published:** 22 Apr 2024

**Academic Editor:** Yuhui Chen **Copy Editor:** Pei-Yun Wang **Production Editor:** Pei-Yun Wang

## Abstract

Sodium-ion batteries (SIBs) are regarded as an outstanding alternative to lithium-ion batteries (LIBs) due to abundant sodium sources and their similar chemistry. As a most promising anode of SIBs, hard carbons (HCs) receive extensive attention because of their low potential and low cost, but their rational design for commercial SIBs is restricted by their variable and complicated microstructure, which is analogous to that of graphite in LIBs. Herein, a series of controllable HC materials derived from 3-aminophenol formaldehyde resin (AFR) were designed and fabricated. We discover that the optimized HC features expanded graphite regions, highly developed nanopores, and reduced defect content, contributing to the enhanced $Na^+$ storage. This optimization is achieved by adjusting the resin crosslinking degree of the precursor. Specifically, a resin precursor with a higher crosslinking degree can produce HC with a larger interlayer distance, relatively higher crystallinity, and a lower specific surface area. Encouragingly, the as-optimized AFR-HC electrode manifests superior electrochemical performance in the aspect of high capacity (383 $mAh \cdot g^{-1}$ at 0.05 $A \cdot g^{-1}$), better rate capability (140 $mAh \cdot g^{-1}$ at 20 $A \cdot g^{-1}$), and high initial coulombic efficiency (82%) than other contrast samples. Moreover, the as-constructed full cell coupled with a $Na_3V_2(PO_4)_3$ cathode shows an energy density of 250 $Wh \cdot kg^{-1}$. Together with the simple synthesis, cost-efficiency of the precursors and superior electrochemical performance, AFR-HCs are promising for the commercial application.

**Keywords:** Sodium-ion batteries, hard carbon, microstructures, 3-aminophenol formaldehyde resin, high rate

## INTRODUCTION

In the past 30 years, lithium-ion batteries (LIBs) have been the state-of-the-art rechargeable batteries and have been extensively used in electric vehicles and mobile electronics[1]. However, the low reserves and high cost of lithium, along with the unsafety, impede their usage in large-scale energy storage systems[2]. Sodium-ion batteries (SIBs), which show similar chemistry to LIBs while being much cheaper, are deemed one of the most promising next-generation energy storage techniques to replace LIBs[3]. Among the various advanced SIB anode materials, hard carbons (HCs) stand out as promising candidates for commercial SIBs by virtue of the abundant active sites for $Na^+$ storage[1], wide sources, and low cost[2]. It has been demonstrated in the literature that a large reversible capacity ranging from 250 to 350 mA·h·g$^{-1}$ can be achieved with HC directly derived from resins, biomass, and pitch[4]. Unfortunately, their reliability toward practical application has been critically questioned, evident in the consistency of electrochemical properties and HC microstructure[1,5]. This could be attributed to the variable and complicated microstructure of HCs.

To this end, various methods for designing HC microstructures are widely employed to address the aforementioned challenges. Specifically, these include (i) expanding the interlayer distance of graphite for accommodating $Na^+$ with large-radius[1]; (ii) adjusting the porous structure to enhance $Na^+$/Na cluster storage within appropriate pores; (iii) introducing heteroatoms[6,7] or defects into the carbon lattice to trigger capacitive adsorption or reactions[6,8,9]; (iv) constructing a favorable carbon form or structure to enhance ion and electron transfer efficiency. Furthermore, the microstructure of HC, including pore structure, defects, and layer spacing, can be controlled by carefully choosing appropriate precursors and adjusting the synthesis and pyrolysis processes. Various types of materials, including phenolic resin (PR)[10,11], pitch[12], anthracite, and biomass[13], are investigated as precursors of HC anodes for SIBs. Among them, PR, which features distinct amorphous graphitic structures and possesses high-purity carbon content compared with other HC precursors, is taken as the most promising SIB anode precursor for real usage[14]. Some pioneers prepared HC spheres from PR precursors with tunable structure in a wide temperature range, in which HC carbonized at 1,900 °C achieved an excellent low-voltage plateau capacity, accounting for 84% of the reversible capacity[15]. However, the design of PR-based HC anodes encounters challenges due to the complicated structure of the precursor and the fussy preparation process. Therefore, the key to achieving high-performance HC anodes for practical applications lies in exploring strategies to regulate the microstructures of HCs and selecting the optimal carbon precursor.

Inspired by the above studies, using 3-aminophenol formaldehyde resin (AFR) as a precursor, we designed and produced various HC materials featuring regular spherical morphology and adjustable microstructure via a simple solution-based routine. Interestingly, we find that the obtained performance of HC shows linear relationship with the crosslinking degree of precursors. In detail, the resin precursor with a higher crosslinking degree could lead to the HC with higher carbon yield, larger $d_{002}$, fewer defects, and lower specific surface area (SSA). The as-optimized AFR-HC material with the highest crosslinking degree features well-regulated nanopores (0.5~2.0 nm), fewer defects [lower ratio of D- to G-band ($I_D/I_G$) of 0.95], decent SSA (11 m$^2$·g$^{-1}$), and larger $d_{002}$ (0.388 nm). These features meet the requirements for $Na^+$ intercalation and Na clustering during charge/discharge processes. As a result, the as-optimized AFR-HC electrode demonstrates a superior reversible capacity of 383 mAh·g$^{-1}$ at 0.05 A·g$^{-1}$, improved rate capability of 140 mAh·g$^{-1}$ at 20 A·g$^{-1}$, and enhanced initial coulombic efficiency (ICE) of 82%, surpassing the control samples. This simple and eco-friendly approach for producing HC could be scalable for regulating different kinds of PR carbons.

## EXPERIMENTAL

### Materials and methods

First, 4 g of 3-aminophenol is dissolved in a mixture of ethanol and water. Then, formaldehyde (37 wt%) is added. The mixed solution was stirred at 70 °C for 1.5 h and then dried at 80 °C for 24 h. Finally, the dried AFR powder was calcined under argon at 1,300 °C to obtain AFR-HCs; the prepared samples were labeled as 0.46-AFR-HC, 0.90-AFR-HC, and 1.80-AFR-HC, respectively.

### Materials characterization

The sample morphologies can be observed using scanning electron microscopy (SEM, Hitachi S-4800). High-resolution transmission electron microscope (HRTEM) and selected area electron diffraction (SAED) images were obtained employing the JEM-2010F transmission electron microscope at 200 kV. X-ray diffraction (XRD) (18 kW D/MAX2500) with Cu Kα radiation (λ = 0.15418 nm) was used to characterize the sample structure; the tube voltage was 40 kV, and the current was 40 mA. The molecular vibration and rotation information of the carbon material was qualitatively analyzed by confocal Raman microscopy (Nanofinder30) with a 532 nm laser excitation. The elemental composition on the surface of the material was measured by the K-alpha X-ray photoelectron spectrometer (XPS) of the German Thermosphere company (voltage:15 kV, current: 15 mA). The elemental analyzer (Vario EL) quantitatively determined the N and O elements in the sample. The SSA and pore information of the material was obtained by Micrometrics ASAP2020 at 77 K.

### Electrochemical measurement

The electrochemical performance of AFR-HCs was tested in 2032-type coin cells using 1 mol/L $NaPF_6$ in diglyme electrolyte, which were assembled in a glove box. The active materials, AFRs, polyvinylidene fluoride (PVDF) and super P with mass ratios of 8:1:1, were then mixed in N-methyl-2-pyrrolidone (NMP). The electrode slurry was coated on a Cu foil. The electrolyte of a full cell is the same as that of a half cell. The capacity ratio of anode/cathode electrodes was 1.2, and the ratio of mass loading between the anode and the cathode was maintained at 1:3; the capacity of the full cell was calculated based on the anode weight loading. The charge-discharge and galvanostatic intermittent titration technique (GITT) test was performed on the Neware CT-4000Q. The diffusivity coefficient of sodium ions ($D_{Na^+}$) is calculated, according to an equation of Fick's second law, by:

$$D = \frac{4}{\pi\tau}\left(\frac{m_B V_M}{M_B S}\right)^2\left(\frac{\Delta E_s}{\Delta E_\tau}\right)^2 \quad (1)$$

Cyclic voltammetry (CV) curve and electrochemical impedance spectroscopy (EIS) tests were carried out using a CHI660 electrochemical workstation.

The specific capacity ($C_t$), specific energy ($E$), and specific power ($P$) of full cells are calculated based on the supplementary equations (2)-(4), where $E$ ($Wh{\cdot}kg^{-1}$) represents the specific energy. $T$ (h) is the total time of the discharge. $C_t$ is the specific capacity of cells. $I$ (mA) is the current of the cell. $P$ ($W{\cdot}kg^{-1}$) is the specific power of the full cell. $U_a$ (V) is the average discharge voltage of the cell, which is calculated from the ratio of specific energy ($E$) to specific capacity ($C_t$). $m_c$ and $m_a$ (kg) are the mass of $Na_3V_2(PO_4)_3$ (NVP) in the cathode and HC in the anode, respectively.

$$C_t = \frac{I \times t}{m_c + m_a} \quad (2)$$

$$E = C_t \times U_a \quad (3)$$

$$P = \frac{E}{t} \quad (4)$$

## RESULTS AND DISCUSSION

### Materials characterization

In this work, the novel AFR sphere was fabricated by the polymerization between 3-aminophenol and formaldehyde; then, a series of HC materials with tailorable microstructures were designed and successfully produced using AFR as a precursor [Figure 1A][3]. The 3-aminophenol molecule contains both phenol and amine groups[15], which reacts with formaldehyde to form benzoxazines and hydroxymethyl derivatives[16]. Next, the benzoxazine and hydroxymethyl derivatives undergo condensation and dehydration to form dimers, which further evolve into polymer chains. Finally, the polymer chains would self-assemble and aggregate to form AFR microspheres. In the reaction, formaldehyde, serving as a curing agent, can interact with 3-aminophenol, and its dosage could further affect the polymerization kinetics of benzoxazine and hydroxymethyl derivatives, thus regulating the crosslinking degree of AFR. Therefore, the crosslinking degree enhancement of AFR can be achieved by increasing the polymerization kinetics induced by the content of formaldehyde, which is realized just by reducing the molar ratio of 3-aminophenol to formaldehyde. The thermogravimetric analysis (TG) was used to evaluate the crosslinking degree of AFR precursors [Figure 1B][10], and the residual carbon rates are 40% for 1.8-AFR-HC, 48% for 0.9-AFR-HC and 58% for 0.46-AFR-HC, respectively. This indicates that a lower molar ratio of aminophenol to formaldehyde leads to a higher crosslinking degree of the resin (0.46-AFR-precursor), eventually resulting in a higher carbon residue rate[11]. It has been reported that the carbon precursors with a higher crosslinking degree could hinder the rapid formation of conjugated carbon network during carbon pyrolysis, thus forming HC with a higher carbon residue rate[14]. The crosslinking degrees for different samples were further analyzed through infrared spectroscopy (IR)[17,18]. As shown in Figure 1C, similar infrared characteristic peaks are illustrated on 0.46-AFR-precursor, 0.90-AFR-precursor and 1.80-AFR-precursor materials, all being pure AFR precursor infrared spectra without redundant peaks. Notably, the main peaks of C=C at 1,610 $cm^{-1}$ and methylene peaks at 1,460 $cm^{-1}$ and 1,480 $cm^{-1}$ are different for 0.46-AFR-precursor, 0.90-AFR-precursor and 1.80-AFR-precursor; the content of methylene and C=C in 0.46-AFR-precursor is higher than both 1.80-AFR-HC and 0.90-AFR-HC[19,20], verifying that the crosslinking degree of AFR precursors can be tuned by the molar ratio of aminophenol to formaldehyde. Further, the peak of C–O–C ether bonds is not obvious, which indicates the polycondensation of 3-aminophenol and formaldehyde is mainly formed by methylene rather than ether bonds[15]. Additionally, the crosslinking degree of the AFR precursor can be further evaluated using a long-term leaching method via a Soxhlet extractor. The productivity of AFR precursors is 92% for 0.46-AFR-precursor, 89% for 0.9-AFR-precursor and 83% for 1.8-AFR-precursor, respectively, which agrees well with the TG and IR results [Figure 1D]. The crosslinking degree of the AFR precursor plays a crucial role in shaping the morphology and microstructure of AFR-HC, suggesting the possibility of ultimately influencing its electrochemical performance [Figure 1E].

As mentioned, the sample morphologies are observable via SEM. As shown in Figure 2A-C, the morphologies of 0.46-AFR-HC, 0.90-AFR-HC and 1.80-AFR-HC samples are all microspheres with a size of around 500 to 900 nm[16]. Notably, the agglomeration degree of HC microspheres gradually increased with rising crosslinking degrees of the resin precursor from 1.80-AFR-HC to 0.46-AFR-HC [Figure 2D-F and Supplementary Figure 1]. This observation supports the influence of the crosslinking degree of resin precursors on the morphology regulation. HRTEM images further display the microstructures of the as-prepared samples [Figure 2G and H]; the 0.46-AFR-HC consists of a short-range ordered graphite domain features with a graphite domain length ($L_a$) of ~2.64 nm, a graphitic crystallite thickness ($L_c$) of ~1.40 nm, and a higher interlayer distance ($d_{002}$) of 0.388 nm. These characteristics are deemed favorable for the intercalation of $Na^+$ ions[2,16]. Additionally, the 0.90-AFR-HC and 1.80-AFR-HC samples illustrate straight short carbon layers featuring the average size of $d_{002}$ (0.384 and 0.372 nm, respectively), the $L_a$ (2.59 and

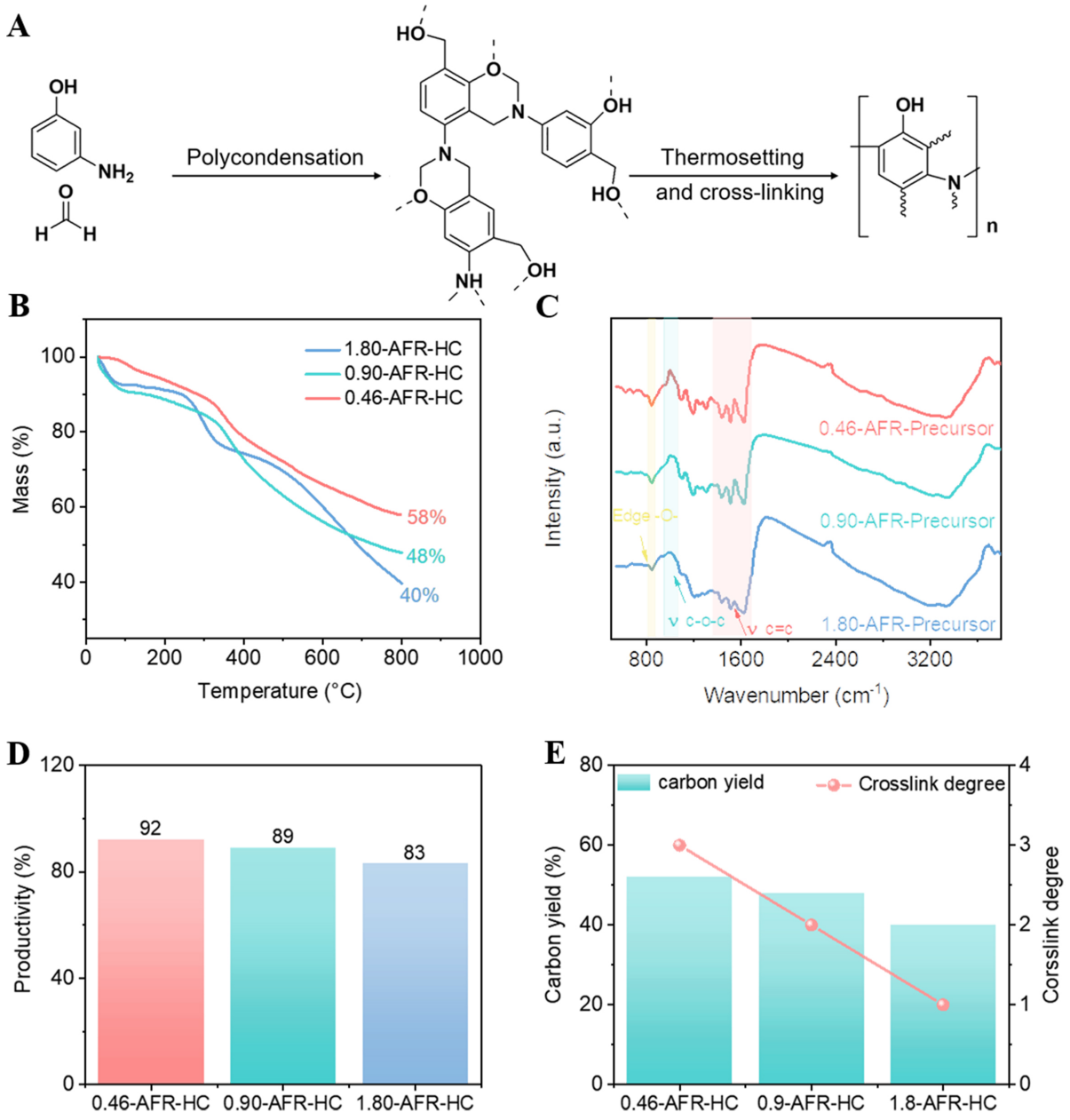


**Figure 1.** (A) Synthesis process of AFR; (B) TG results; (C) IR spectroscopy; (D) The yield of different samples was tested by a long-term leaching method; (E) Comparison of carbon yield and crosslinking degree. AFR: Aminophenol formaldehyde resin; TG: thermogravimetric analysis; IR: infrared spectroscopy.

2.56 nm, respectively), and the $L_c$ (1.36 and 1.32 nm, respectively) [Figure 2H and I, Supplementary Table 1]. Elemental mapping by energy-dispersive X-ray spectroscopy (EDS) of 0.46-AFR-HC, 0.90-AFR-HC and 1.80-AFR-HC samples [Figure 2J, Supplementary Figure 2A and B] also show a uniform distribution of C, N and O.

The XRD can be performed to evaluate the graphitization degree and the microstructure parameters of HC materials[21-24]. The XRD patterns of all AFR-HC materials show typical HC characteristic peaks at ≈23° and ≈42°, which are attributed to the (002) and (100) planes of HC, respectively [Figure 3A and Supplementary

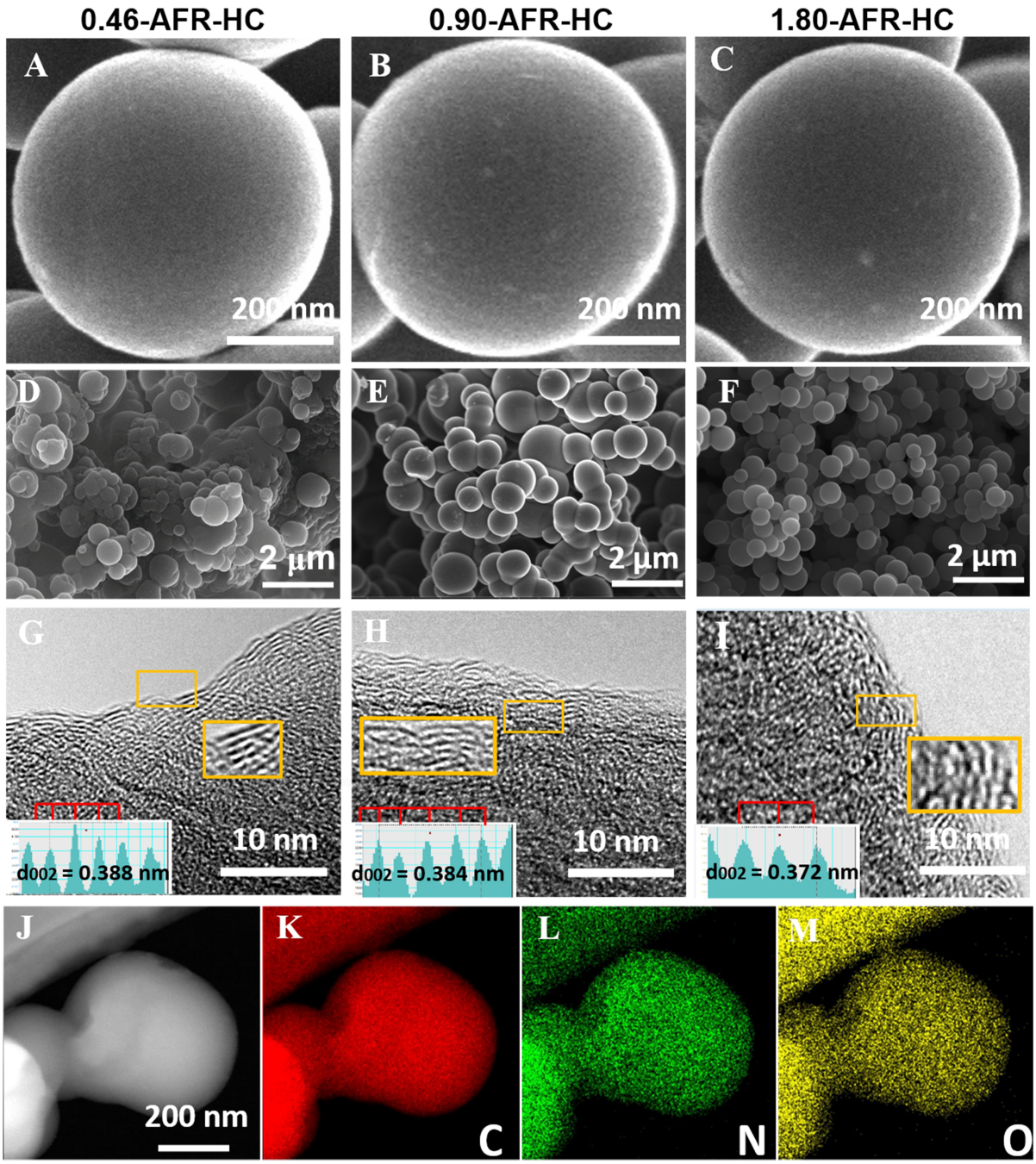


**Figure 2.** (A-F) SEM images; (G-I) HRTEM images; (J-M) EDS mappings of 0.46-AFR-HC, the (K), (L), and (M) figures belong to the EDS mappings of C, N and O elements respectively. SEM: Scanning electron microscopy; HRTEM: high-resolution transmission electron microscope; EDS: Energy dispersive spectrometer; AFR: aminophenol formaldehyde resin; HC: hard carbon.

Figure 3][25]. Surprisingly, the calculated $d_{002}$ is 0.401 nm for 0.46-AFR-HC, 0.389 nm for 0.9-AFR-HC, and 0.374 nm for 1.8-AFR-HC, respectively. Additionally, the $L_c$ gradually shifts toward higher values and $L_a$ shifts toward lower values with an increasing resin precursor crosslinking degree. For example, 0.46-AFR-HC, 0.90-AFR-HC, and 1.80-AFR-HC samples feature with the $L_a$ (3.01, 2.89, and 2.88 nm, respectively) and the $L_c$ (1.46, 1.42, and 1.33 nm, respectively) are summarized in Supplementary Table 1. All these results are consistent with the TEM results [Figure 2G-I].

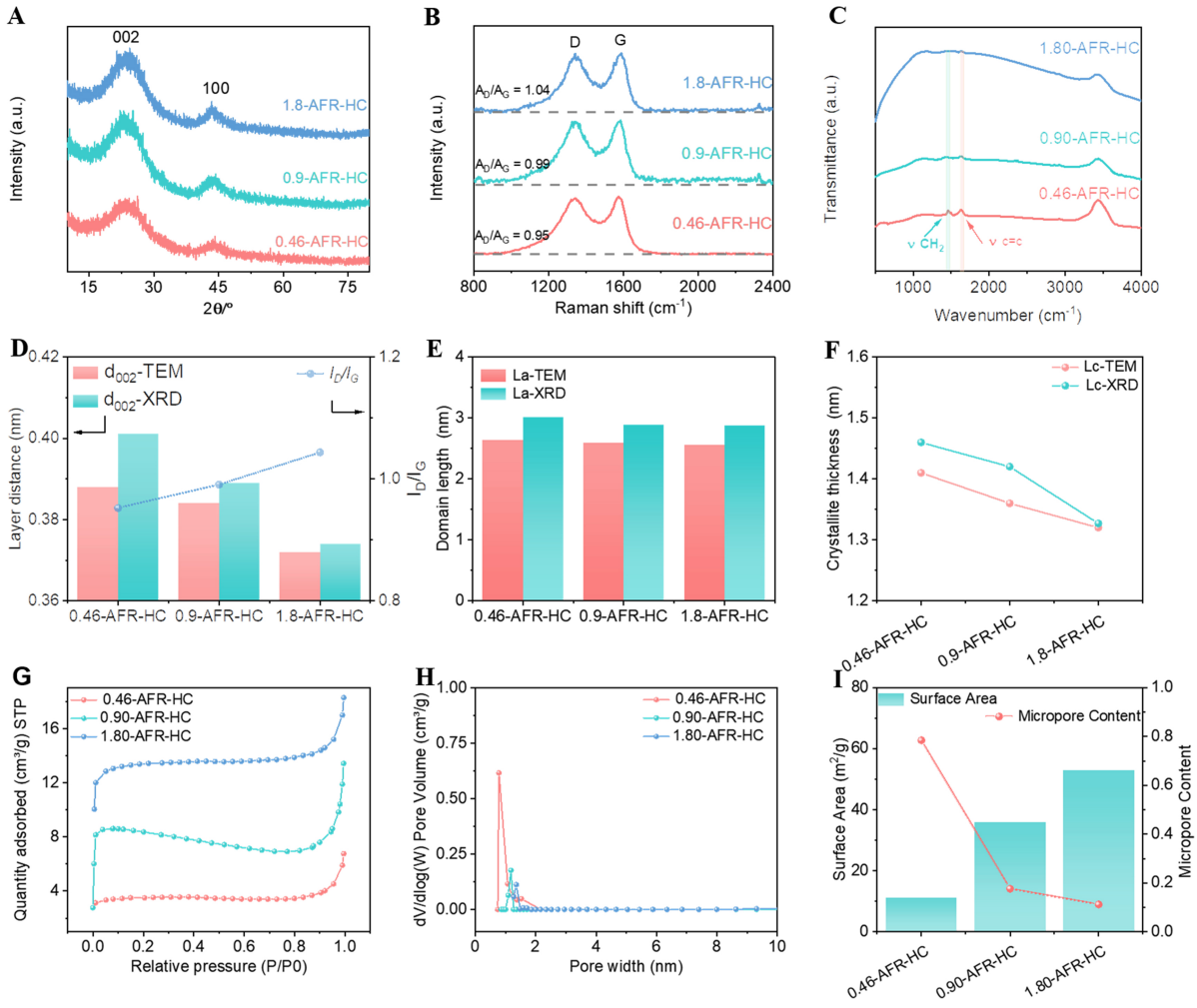


**Figure 3.** (A) XRD patterns; (B) Raman spectra; (C) FTIR spectroscopy; (D) Comparison of $d_{002}$ and $I_D/I_G$; (E and F) Comparison of $L_a$ and $L_c$; (G) $N_2$ adsorption-desorption isotherms at 77 K; (H) Pore diameter distributions based on $N_2$ adsorption-desorption isotherms; (I) Comparison of surface area and micropore content. XRD: X-ray diffraction; FTIR: Fourier transform infrared spectroscopy.

The microcrystalline variations of different samples are also confirmed by the Raman spectrum[26]. As shown in Figure 3B, the Raman plots of 0.66-AFR-HC, 0.90-AFR-HC and 1.80-AFR-HC all contain two characteristic bands of 1,350 cm$^{-1}$ (D band) and 1,590 cm$^{-1}$ (G band), which correspond to the characteristic peaks of disordered or defective graphite ($sp^3$) and crystalline graphite ($sp^2$), respectively[25,27]. Specifically, the Raman band can be fitted into four peaks located at 1,240, 1,350, 1,500, and 1,590 cm$^{-1}$, identified as D1, D, D2, and G, respectively [Supplementary Figure 4]. The D1 band (~1,240 cm$^{-1}$) is assigned to the disordered graphitic lattice of the stretching vibrations of a mixture of $sp^2$–$sp^3$ or $sp^3$ bonds[21]. The D2 band (~1,500 cm$^{-1}$) represents the amorphous carbon[21]. It should be noted that the $I_D/I_G$ represents the defect degree of HC, and its values are decreased in the order of 1.80-AFR-HC (1.043), 0.90-AFR-HC (0.99), and 0.46-AFR-HC (0.95) [Figure 3B and Supplementary Table 2], revealing that the defect degree of AFR-HC decreases slightly with the crosslinking degree of a precursor. The as-optimized 0.46-AFR-HC with a short-range ordered structure could be considered favorable for higher ICE. Fourier transform IR (FTIR) presents a similar trend to the Raman spectrum [Figure 3C][4]; intensity of methylene (1,460

and 1,480 $cm^{-1}$) and C=C (1,610 $cm^{-1}$) peaks in 0.46-AFR-HC is higher than both 1.80-AFR-HC and 0.90-AFR-HC. This indicates higher crystallinity HCs can be obtained by increasing the crosslinking degree of the precursor. The microstructure parameters for all the samples were further summarized in Figure 3D-F, Supplementary Tables 1 and 2.

$N_2$ adsorption was used to detect pore structure and SSA of HC [Figure 3G and H, Supplementary Table 3][28,29]. Interestingly, the crosslinking degrees of AFR-precursors directly affect the SSA and the nanopore structure of HC[25]. The SSA values are 11.18 $m^2 \cdot g^{-1}$ for 0.46-AFR-HC, 35.73 $m^2 \cdot g^{-1}$ for 0.9-AFR-HC, and 52.89 $m^2 \cdot g^{-1}$ for 1.8-AFR-HC, respectively. This indicates that the SSA of AFR-derived HC decreases as the precursor crosslinking degree increases. Notably, the micropore sizes of 0.46-AFR-HC mainly distributed from 0.5 to 2.0 nm while exhibiting a lower surface area [Figure 3H and Supplementary Table 3]. This indicates that as the crosslinking degree of the precursor increases, a substantial portion of the open pores in 0.46-AFR-HC becomes covered, leading to a higher proportion of closed pores and a lower surface area[14,16]. The moderate SSA and increased number of closed pores contribute to the higher ICE and capacity of electrodes[16,29].

XPS was employed to characterize the chemical composition and elemental state of the samples [Supplementary Figures 5-8][3]. The full spectra demonstrate that the samples of 0.46-AFR-HC, 0.90-AFR-HC, and 1.80-AFR-HC are mainly composed of C, O, and N elements [Supplementary Figure 5], however, with varying contents. It is noteworthy that 0.46-AFR-HC shows an increase in carbon content (93.29 at%) compared to 0.90-AFR-HC (92.63 at%) and 1.8-AFR-HC (92.07%) samples [Supplementary Table 4], indicating that the carbon content and the compaction density of HC could be regulated by varying the crosslinking degree of the precursor [Supplementary Table 5]. It has been proven that anode materials with a higher compaction density would benefit the construction of high energy density electrodes[28-31].

All these observations illuminate the connection between the structures of the precursor and the local microstructure of the obtained HC. Notably, the optimized 0.46-AFR-HC exhibits short-order carbon layers with a larger $d_{002}$ value, appropriate crystallinity, well-defined micropores, and lower SSA. These characteristics are deemed favorable for the $Na^+$ filling in micropores and intercalation in graphite layers [Figure 3I][32-35].

### Sodium storage performance

The electrochemical performances of the AFR-HCs were tested using Na||AFR-HC half cells in diglyme-based electrolytes[31,32]. Obviously, the 0.46-AFR-HC electrode demonstrates a salient enhancement in the reversible capacity, ICE and rate capability. The galvanostatic charge/discharge curves (GCDs) of the first cycle for AFR-HCs show a representative charge and discharge process of HC, which display a slope region above 0.1 V and a plateau region below 0.1 V [Figure 4A][10,36-38]. During the first cycle, the discharge/charge capacities are 383/547, 348/440, and 271/363 $mAh \cdot g^{-1}$ at 0.05 $A \cdot g^{-1}$ for 0.46-AFR-HC, 0.90-AFR-HC, and 1.80-AFR-HC electrodes, causing the ICE of 82%, 79%, and 73%, respectively [Figure 4A][37]. The superior capacity and ICE could be related to the well-regulated microstructure and smallest surface area of 0.46-AFR-HC.

Moreover, rate performance was also conducted [Figure 4B], and the corresponding GCD curves at different rates are shown in Supplementary Figure 9. Clearly, 0.46-AFR-HC displays reversible capacities of 383, 253, and 203 $mAh \cdot g^{-1}$ at current densities of 0.1, 5.0, and 10.0 $A \cdot g^{-1}$, respectively, far exceeding 0.90-AFR-HC and 1.80-AFR-HC electrodes. Even at a large current density as high as 20 $A \cdot g^{-1}$, 0.46-AFR-HC still can deliver the discharge capacity of 140 $mAh \cdot g^{-1}$, indicating that the well-regulated 0.46-AFR-HC is

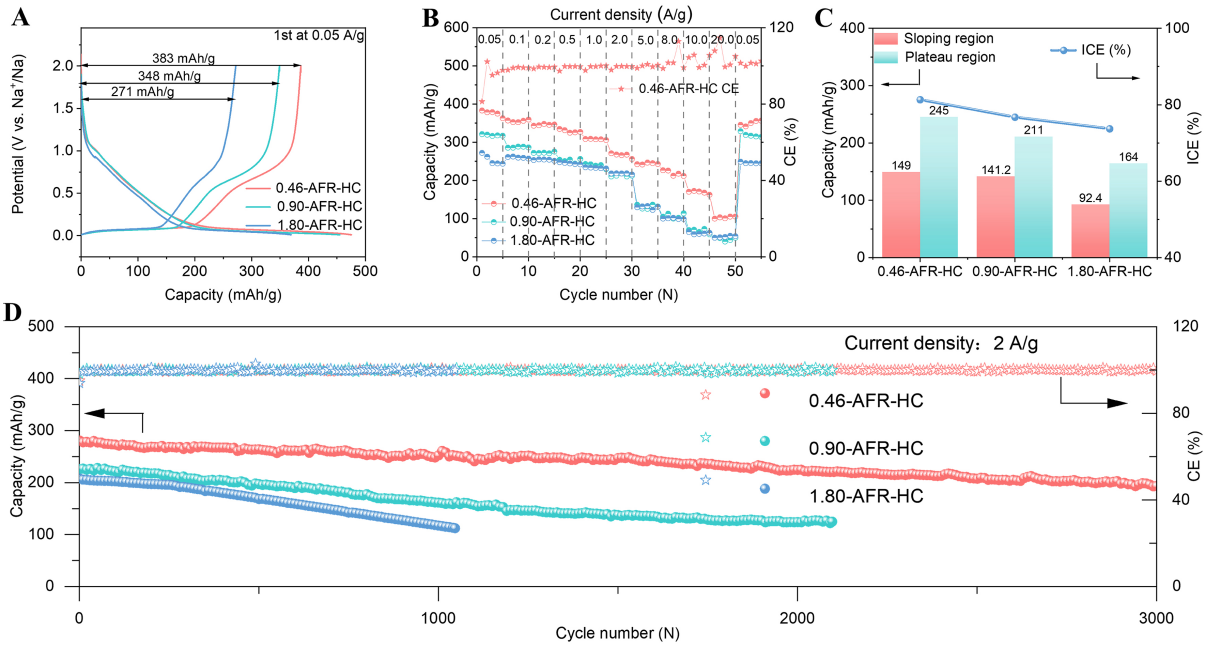


**Figure 4.** (A) The discharge-charge curves at the first cycle; (B) Rate performances; (C) Comparison of ICE and plateau/sloping capacities; (D) Cycling stability. ICE: Initial coulombic efficiency.

beneficial for fast $Na^+$ reaction kinetics. Importantly, the plateau capacity ratio of 0.46-AFR-HC is retained by 62% (245 mAh·$g^{-1}$) at 0.05 A·$g^{-1}$, while the proportions are retained by 59% and 56% in 0.90-AFR-HC (211 mAh·$g^{-1}$) and 1.80-AFR-HC (164 mAh·$g^{-1}$) [Figure 4C], and the larger plateau region ratio would be advantageous for the construction of the full cell[33]. Furthermore, after 1,000 cycles, the 0.46-AFR-HC electrode still exhibits a specific capacity of 268.4 mAh·$g^{-1}$ at 2 A·$g^{-1}$ with a high capacity retention of 94% [Figure 4D], correlating well with the SEM and TEM images for 0.46-AFR-HC after cycles [Supplementary Figures 10 and 11]. This is significantly improved compared with 0.90-AFR-HC for 70% (158.2 mAh·$g^{-1}$ at 2 A·$g^{-1}$) and 1.80-AFR-HC for 54% (115.3 mAh·$g^{-1}$ at 2 A·$g^{-1}$) after 1,000 cycles. To investigate the superiority of the AFR-HC on sodium storage behavior, the other types of half cells were also assembled, using pitch-based HC[7,12] and biomass-based HC[35,36] as anodes and sodium metal foil as counter electrodes. Among these materials, 0.46-AFR-HC possesses the highest rate capacity of 253 mAh·$g^{-1}$ under 5 A·$g^{-1}$ compared with biomass-based HC (54 mAh·$g^{-1}$ at 5 A·$g^{-1}$, Supplementary Figure 12A and B, Supplementary Tables 6 and 7) and pitch-based HC (50 mAh·$g^{-1}$ at 5 A·$g^{-1}$). The high capacity, rate capability, cycling stability, and ICE exhibited by 0.46-AFR-HC outperform the control samples and other types of HCs, indicating that 0.46-AFR-HC is a promising anode material for SIBs[37].

### Sodium storage behavior exploration and the microstructural parameters-performance

The better electrochemical performances regarding rate performance, capacity and cyclic stability make 0.46-AFR-HC electrodes promising for practical SIBs and, meanwhile, prompt us to explore their kinetics behavior. CV tests were conducted to reveal the Na storage behavior of 0.46-AFR-HC, 0.90-AFR-HC and 1.80-AFR-HC samples within charge/discharge processes (0.01~2.0 V)[15]. In Supplementary Figure 13, a distinctive sharp peak at ≈0.1 V observed at 0.2 mV·$s^{-1}$ belongs to the plateau region (< 0.1 V)[39]. This can be attributed to the $Na^+$ filling in micropores and intercalation in graphite layers[1]. The enhanced rate capability of the AFR-0.46-HC electrode is evident from the CV curves[24]. Notably, the decision step of kinetic behavior for the interface reaction was assessed by applying the equation $I = av^b$ to fit the $b$ values, a commonly used approach for kinetic evaluation[24,40]. In Supplementary Figures 14 and 15, excellent linear fit

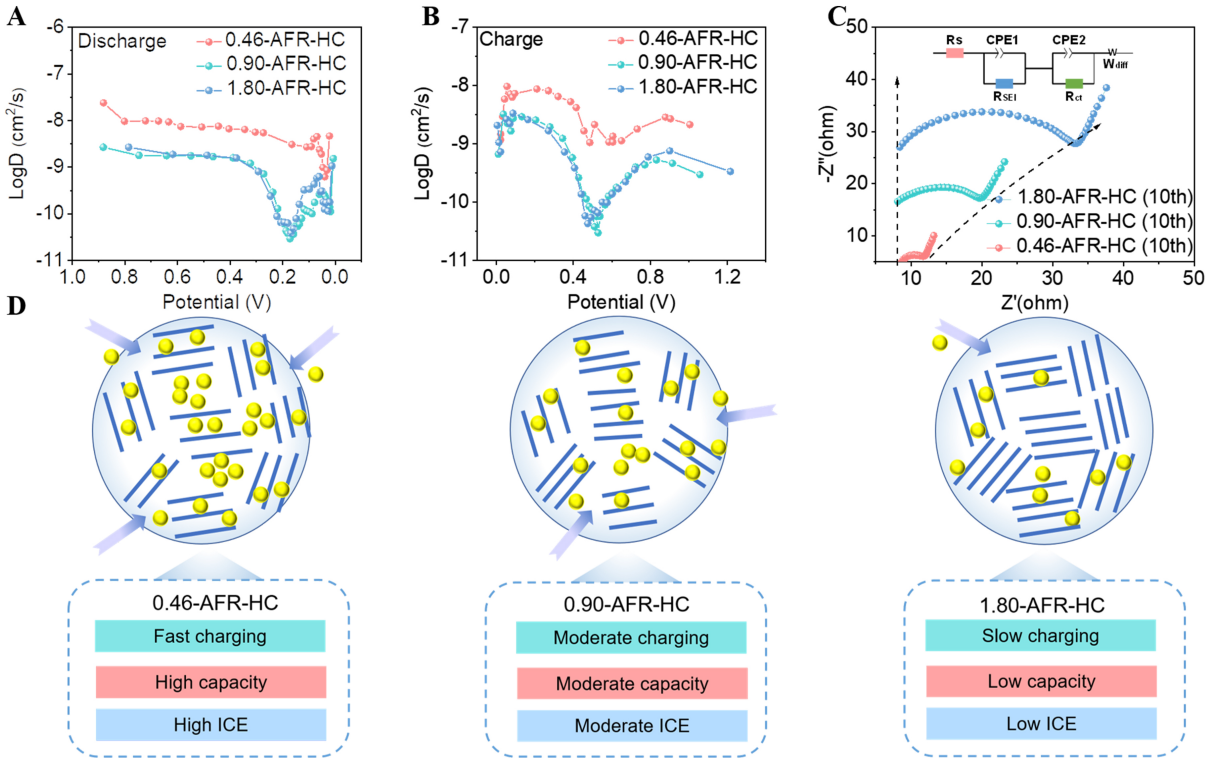


**Figure 5.** (A and B) $Na^+$ diffusion coefficients calculated from the GITT potential profiles under discharge/charge processes; (C) EIS analysis after ten cycles; (D) Sodium storage diagram of AFR-HCs. GITT: Galvanostatic intermittent titration technique; EIS: electrochemical impedance spectroscopy; AFR: aminophenol formaldehyde resin; HCs: hard carbons.

results are observed for all three samples; the fitted *b* value for 0.46-AFR-HC (0.58) is larger than that for 0.90-AFR-HC (0.56) and 1.80-AFR-HC (0.55) [Supplementary Figure 15A-C]. The *b* value is between 0.5 and 1.0. This means that both diffusion control and capacitance processes may contribute to the charge storage of 0.46-AFR-HC[24,30].

Furthermore, a GITT test was performed to further analyze sodium ion diffusion coefficients ($D_{Na^+}$) in 0.46-AFR-HC, 0.90-AFR-HC and 1.80-AFR-HC electrodes[36,39]. It was found that the $D_{Na^+}$ values of the 0.46-AFR-HC electrode ($10^{-7.81}$ to $10^{-9.50}$) are higher than the 0.90-AFR-HC ($10^{-8.75}$ to $10^{-10.54}$) and 1.80-AFR-HC ($10^{-8.64}$ to $10^{-10.47}$) at all potentials, especially in the low voltage region ($10^{-9.50}$ *vs.* $10^{-10.54}$ *vs.* $10^{-10.47}$) [Figure 5A and B]. The incredible enhancement of $D_{Na^+}$ in 0.46-AFR-HC at all potentials could also explain its better rate performance[3]. Such superior electrochemical performance could be derived from the well-regulated 0.46-AFR-HC microstructure. To gain insight into the interfacial reaction kinetics of 0.46-AFR-HC, 0.90-AFR-HC, and 1.80-AFR-HC electrodes, the EIS measurements were performed[37,41]. Selected Nyquist plots for these samples are presented in Figure 5C[37]. These results indicate that the resistances originating from the solid electrolyte interphase (SEI) layer ($R_{SEI}$) and charge transfer ($R_{ct}$) in 0.46-AFR-HC electrodes are both lower than those in 0.90-AFR-HC and 1.80-AFR-HC electrodes[36,39,41], that is, 2.6 Ω *vs.* 3.9 Ω *vs.* 7.3 Ω for $R_{SEI}$ and 3.6 Ω *vs.* 7.9 Ω *vs.* 11.8 Ω for $R_{ct}$, respectively [Supplementary Table 8].

We conclude that the enhanced electrochemical performance of 0.46-AFR-HC can be attributed to its ideal microstructure. Firstly, there is a certain linear relationship between the resin crosslinking degree of a precursor and the microstructure of as-obtained HC; that is, the greater the degree of resin crosslinking, the higher carbon yield, the higher graphitization degree, the larger $d_{002}$ and lower SSA. Promisingly, the

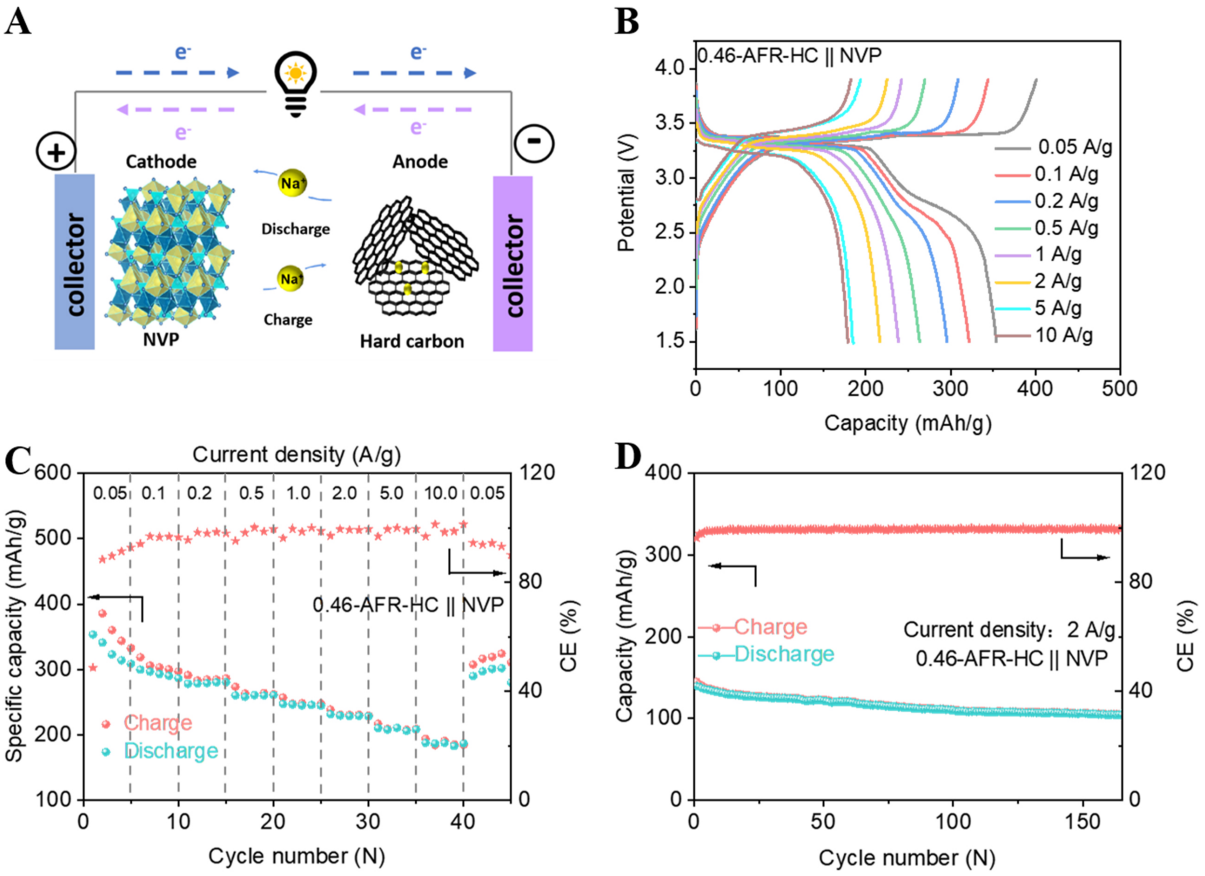


**Figure 6.** (A) Schematic of sodium-ion full-cell; (B) The GCD profiles under different rates; (C) Rate performance; (D) Cycling stability. GCD: Galvanostatic charge/discharge curve.

optimized 0.46-AFR-HC material features well-regulated microstructures (0.5~2.0 nm), less defect (lower $I_D/I_G$ of 0.95), lower SSA (11 $m^2 \cdot g^{-1}$), and larger $d_{002}$ (0.388 nm). These characteristics fulfill the requirements for the intercalation and Na clustering of $Na^+$ during charge and discharge processes [Figure 5D].

### Electrochemical performance of AFR-HC||NVP full cell

Full cells were assembled to further verify the practical application of 0.46-AFR-HC material; the full-cell configuration is shown in Figure 6A, and NVP is selected as a cathode[36]. Before assembling the full cell, the 0.46-AFR-HC anode first underwent pre-sodium through an electrochemical process to facilitate the formation of the SEI[42,43]. The full cell shows a high charge capacity of 365 $mAh \cdot g^{-1}$ at 0.05 $A \cdot g^{-1}$ (based on the active mass of the anode material, Figure 6B)[1], with a specific energy density of 256 $Wh \cdot kg^{-1}$. Furthermore, it delivers good rate performance, maintaining a capacity of 158 $mAh \cdot g^{-1}$ at 10 $A \cdot g^{-1}$ [Figure 6C]. This corresponds to a power density of 6.43 $kW \cdot kg^{-1}$. Additionally, it exhibits stable capacity over 200 cycles, maintaining approximately 110 $mAh \cdot g^{-1}$ at 2 $A \cdot g^{-1}$ (80% capacity retention) [Figure 6D]. As a result, the superior sodium storage properties of 0.46-AFR-HC in half/full cells illustrate that it is a promising carbon material and can be used in SIBs.

## CONCLUSIONS

In summary, we have fabricated a AFR-based HC material with better performance, higher ICE and capacity than other control samples by adjusting the crosslinking degree of the AFR precursor. The 0.46-

AFR-HC electrode presents higher reversible capacity (383 mAh·$g^{-1}$ at 0.05 A·$g^{-1}$), ICE (82%) and good rate capability (140 mAh·$g^{-1}$ at 20 A·$g^{-1}$) compared to the control samples and other types of HCs. Further, the full cell with 0.46-AFR-HC as an anode and NVP as a cathode demonstrates high energy/power densities of 250 Wh·$kg^{-1}$ and 6.43 kW·$kg^{-1}$, respectively. The superior electrochemical performance observed in the experiment can be attributed to the consistency between the crosslinking degree of the precursor and the microstructure parameters of HC. Specifically, a resin precursor with a higher crosslinking degree tends to produce the optimized 0.46-AFR-HC with higher carbon yield, a larger $d_{002}$, fewer defects, and a lower surface area. These characteristics are deemed promising for constructing high-performance anode materials. This work proposes a reliable design for high performance HCs and provides a simple and eco-friendly method to prepare HCs with an ideal microstructure in large quantities.

## DECLARATIONS

### Authors' contributions

Wrote the article: Lu Z

Made substantial contributions to conception and design of the study and performed data analysis and interpretation: Lu Z, Yin X

Performed experiment: Ji Y, Li C, Wang R, Li S, Yuan T

Performed data acquisition and provided administrative, technical, and material support: Zhao Y

### Availability of data and materials

Supporting information is available from the authors.

### Financial support and sponsorship

This work is supported by the National Natural Science Foundation of China (22179077), National Natural Science Foundation Youth Fund (22209104), Shanghai Science and Technology Commission's "2020 Science and Technology Innovation Action Plan" (20511104003), and Natural Science Foundation in Shanghai (21ZR1424200).

### Conflicts of interest

All authors declared that there are no conflicts of interest.

### Ethical approval and consent to participate

Not applicable.

### Consent for publication

Not applicable.



## REFERENCES

1. Lu Z, Wang J, Feng W, et al. Zinc single-atom-regulated hard carbons for high-rate and low-temperature sodium-ion batteries. *Adv Mater* 2023;35:2211461. DOI PubMed
2. Sun N, Guan Z, Liu Y, et al. Extended "adsorption–insertion" model: a new insight into the sodium storage mechanism of hard carbons. *Adv Energy Mater* 2019;9:1901351. DOI
3. Yin X, Lu Z, Wang J, et al. Enabling fast $Na^+$ transfer kinetics in the whole-voltage-region of hard-carbon anodes for ultrahigh-rate sodium storage. *Adv Mater* 2022;34:2109282. DOI PubMed
4. Liu G, Wang Z, Yuan H, et al. Deciphering electrolyte dominated $Na^+$ storage mechanisms in hard carbon anodes for sodium-ion batteries. *Adv Sci* 2023;10:2305414. DOI PubMed PMC
5. Komaba S, Murata W, Ishikawa T, et al. Electrochemical Na insertion and solid electrolyte interphase for hard-carbon electrodes and

application to Na-ion batteries. *Adv Funct Mater* 2011;21:3859-67. DOI
6. Lu H, Ai F, Jia Y, et al. Exploring sodium-ion storage mechanism in hard carbons with different microstructure prepared by ball-milling method. *Small* 2018;14:1802694. DOI
7. Liu Y, Lu YX, Xu YS, et al. Pitch-derived soft carbon as stable anode material for potassium ion batteries. *Adv Mater* 2020;32:2000505. DOI
8. Li Z, Chen Y, Jian Z, et al. Defective hard carbon anode for Na-ion batteries. *Chem Mater* 2018;30:4536-42. DOI
9. Yin B, Liang S, Yu D, et al. Increasing accessible subsurface to improving rate capability and cycling stability of sodium-ion batteries. *Adv Mater* 2021;33:2100808. DOI PubMed
10. Fan C, Zhang R, Luo X, et al. Epoxy phenol novolac resin: a novel precursor to construct high performance hard carbon anode toward enhanced sodium-ion batteries. *Carbon* 2023;205:353-64. DOI
11. Beda A, Taberna PL, Simon P, Matei Ghimbeu C. Hard carbons derived from green phenolic resins for Na-ion batteries. *Carbon* 2018;139:248-57. DOI
12. Yin X, Zhao Y, Wang X, et al. Modulating the graphitic domains of hard carbons derived from mixed pitch and resin to achieve high rate and stable sodium storage. *Small* 2022;18:2105568. DOI
13. Wu L, Buchholz D, Vaalma C, Giffin GA, Passerini S. Apple-biowaste-derived hard carbon as a powerful anode material for Na-ion batteries. *ChemElectroChem* 2016;3:292-8. DOI
14. Kamiyama A, Kubota K, Nakano T, et al. High-capacity hard carbon synthesized from macroporous phenolic resin for sodium-ion and potassium-ion battery. *ACS Appl Energy Mater* 2020;3:135-40. DOI
15. Zha X, Chen Y, Fan H, et al. Handedness inversion of chiral 3-aminophenol formaldehyde resin nanotubes mediated by metal coordination. *Angew Chem Int Ed Engl* 2021;60:7759-69. DOI
16. Zhao J, Gilani MRHS, Lai J, et al. Autocatalysis synthesis of poly(benzoxazine-*co*-resol)-based polymer and carbon spheres. *Macromolecules* 2018;51:5494-500. DOI
17. Zhang X, Dong X, Qiu X, et al. Extended low-voltage plateau capacity of hard carbon spheres anode for sodium ion batteries. *J Power Sources* 2020;476:228550. DOI
18. Li Q, Liu X, Tao Y, et al. Sieving carbons promise practical anodes with extensible low-potential plateaus for sodium batteries. *Natl Sci Rev* 2022;9:nwac084. DOI PubMed PMC
19. Wang H, Sun F, Qu Z, et al. Oxygen functional group modification of cellulose-derived hard carbon for enhanced sodium ion storage. *ACS Sustain Chem Eng* 2019;7:18554-65. DOI
20. Yi Z, Zhang J, Zhang S, Gao Q, Li J, Zhang W. Synthesis and mechanism of metal-mediated polymerization of phenolic resins. *Polymers* 2016;8:159. DOI PubMed PMC
21. Cheng D, Zhou X, Hu H, et al. Electrochemical storage mechanism of sodium in carbon materials: a study from soft carbon to hard carbon. *Carbon* 2021;182:758-69. DOI
22. Gomez-martin A, Martinez-fernandez J, Ruttert M, Winter M, Placke T, Ramirez-Rico J. Correlation of structure and performance of hard carbons as anodes for sodium ion batteries. *Chem Mater* 2019;31:7288-99. DOI
23. Li Y, Xu S, Wu X, et al. Amorphous monodispersed hard carbon micro-spherules derived from biomass as a high performance negative electrode material for sodium-ion batteries. *J Mater Chem A* 2015;3:71-7. DOI
24. Alvin S, Yoon D, Chandra C, et al. Extended flat voltage profile of hard carbon synthesized using a two-step carbonization approach as an anode in sodium ion batteries. *J Power Sources* 2019;430:157-68. DOI
25. Xia JL, Yan D, Guo LP, Dong XL, Li WC, Lu AH. Hard carbon nanosheets with uniform ultramicropores and accessible functional groups showing high realistic capacity and superior rate performance for sodium-ion storage. *Adv Mater* 2020;32:2000447. DOI PubMed
26. Nazarian-Samani M, Nazarian-Samani M, Haghighat-Shishavan S, Kim KB. Efficient stress alleviation and interface regulation in $Cu_4SiP_8$-CNT hybrid for ultra-durable Li and Na storage. *Nano Energy* 2021;86:106134. DOI
27. Rebelo SLH, Guedes A, Szefczyk ME, Pereira AM, Araújo JP, Freire C. Progress in the Raman spectra analysis of covalently functionalized multiwalled carbon nanotubes: unraveling disorder in graphitic materials. *Phys Chem Chem Phys* 2016;18:12784-96. DOI PubMed
28. Jurkiewicz K, Pawlyta M, Zygadło D, et al. Evolution of glassy carbon under heat treatment: correlation structure-mechanical properties. *J Mater Sci* 2018;53:3509-23. DOI
29. Morikawa Y, Nishimura S, Hashimoto R, Ohnuma M, Yamada A. Mechanism of sodium storage in hard carbon: an X-ray scattering analysis. *Adv Energy Mater* 2020;10:1903176. DOI
30. Sun F, Wang H, Qu Z, et al. Carboxyl-dominant oxygen rich carbon for improved sodium ion storage: synergistic enhancement of adsorption and intercalation mechanisms. *Adv Energy Mater* 2021;11:2002981. DOI
31. Kamiyama A, Kubota K, Igarashi D, et al. MgO-template synthesis of extremely high capacity hard carbon for Na-ion battery. *Angew Chem Int Ed Engl* 2021;60:5114-20. DOI PubMed PMC
32. Liu M, Wu F, Gong Y, et al. Interfacial-catalysis-enabled layered and inorganic-rich SEI on hard carbon anodes in ester electrolytes for sodium-ion batteries. *Adv Mater* 2023;35:2300002. DOI
33. Tang Z, Zhang R, Wang H, et al. Revealing the closed pore formation of waste wood-derived hard carbon for advanced sodium-ion battery. *Nat Commun* 2023;14:6024. DOI PubMed PMC
34. Zhong J, Wang T, Wang L, et al. A silicon monoxide lithium-ion battery anode with ultrahigh areal capacity. *Nanomicro Lett*

2022;14:50. DOI PubMed PMC

35. Billaud J, Bouville F, Magrini T, Villevieille C, Studart AR. Magnetically aligned graphite electrodes for high-rate performance Li-ion batteries. *Nat Energy* 2016;1:16097. DOI
36. Wu F, Zhang M, Bai Y, Wang X, Dong R, Wu C. Lotus seedpod-derived hard carbon with hierarchical porous structure as stable anode for sodium-ion batteries. *ACS Appl Mater Interfaces* 2019;11:12554-61. DOI
37. Wang Q, Zhu X, Liu Y, Fang Y, Zhou X, Bao J. Rice husk-derived hard carbons as high-performance anode materials for sodium-ion batteries. *Carbon* 2018;127:658-66. DOI
38. Alvin S, Cahyadi HS, Hwang J, Chang W, Kwak SK, Kim J. Revealing the intercalation mechanisms of lithium, sodium, and potassium in hard carbon. *Adv Energy Mater* 2020;10:2000283. DOI
39. Dong R, Zheng L, Bai Y, et al. Elucidating the mechanism of fast Na storage kinetics in ether electrolytes for hard carbon anodes. *Adv Mater* 2021;33:2008810. DOI
40. Chen C, Huang Y, Zhu Y, et al. Nonignorable influence of oxygen in hard carbon for sodium ion storage. *ACS Sustain Chem Eng* 2020;8:1497-506. DOI
41. Han J, Johnson I, Lu Z, Kudo A, Chen M. Effect of local atomic structure on sodium ion storage in hard amorphous carbon. *Nano Lett* 2021;21:6504-10. DOI PubMed
42. Dong X, Wang X, Lu Z, et al. Construction of Cu-Zn Co-doped layered materials for sodium-ion batteries with high cycle stability. *Chin Chem Lett* 2024;35:108605. DOI
43. Cheng SL, Yin XP, Sarkar S, et al. A novel $Mo_{8.7}Nb_{6.1}O_x$@NCs egg-nest composite structure as superior anode material for lithium-ion storage. *Rare Met* 2022;41:2645-54. DOI